# Inverse-Designed Tellurite Devices for Polarization Control

Julian L. Pita, Jorge Diego Marconi, and Michaël Ménard, *Member, IEEE*

***Abstract*—Tellurite glasses are of high interest in integrated photonics for sensing and, in particular, telecommunications applications, where they serve as key materials for amplification and mid-IR light sources due to their wide transparent window, thermal and mechanical stability, and high optical nonlinearity. In this work, we present two inverse-designed devices for polarization management on a tellurium dioxide platform: a TM-pass polarizer and a polarization beam splitter. The TM-pass polarizer achieves an average simulated transmission efficiency of −0.6 dB and an polarization crosstalk below −20.9 dB across the entire C-band, with a footprint of only 24 $\mu$m × 6 $\mu$m. The polarization beam splitter has an ultra-compact footprint of 28 $\mu$m × 6 $\mu$m and achieves average TE and TM transmission efficiencies of approximately −0.4 dB, with crosstalk below −18.3 dB and −27.2 dB, respectively. These are the first freeform devices demonstrated on a tellurium dioxide platform, exhibiting strong robustness to fabrication variations and showcasing the versatility of the platform beyond nonlinear applications.**

***Index Terms*—Tellurite photonics, integrated optics, polarization control.**

## I. INTRODUCTION

FOR centuries, glasses have been widely used in various scientific and technical applications [1]. In recent decades, glasses with high transparency in the visible and infrared spectral regions—from approximately 0.4 $\mu$m to 20 $\mu$m—including chalcogenides, oxides, and nitrides, have attracted significant attention for their potential in photonic devices [2], [3], [4], particularly those related to data transmission applications. Among these, tellurium oxide composite glasses (tellurite or $TeO_2$ glasses) stand out as a particularly promising option. Beyond their wide spectral transparency, they offer several advantageous properties, including high nonlinear refractive indices, low material dispersion, good thermal and mechanical stability, corrosion resistance, and a low melting point [4], [5].

Tellurite glasses are well known for their high solubility of rare earth ions. When doped or co-doped with ions such as $Er^3+$, $Ho^3+$, $Pr^3+$, and $Yb^3+$, they demonstrate excellent performance in active devices, including optical amplifiers and lasers [6], [7]. In addition, the high nonlinear refractive index of $TeO_2$ can be exploited for all-optical switching [8], as well as for nonlinear optical devices based on tellurite glass fibers, including optical parametric amplifiers, wavelength converters, and supercontinuum generators [9], [10], [11].

High-quality, low-loss tellurite glasses have been achieved by minimizing impurity sources during the fabrication process, reaching losses as low as 0.001 dB/cm in bulk samples [12]. Thin films have also been demonstrated, exhibiting very low losses with an imaginary refractive index of $k < 10^{-4}$ at 1550 nm [13]. These properties make tellurite an attractive material for integrated photonic devices, particularly when embedded in or surrounded by silicon dioxide, enabling potential compatibility with silicon-on-insulator (SOI) and silicon nitride platforms [5], [14]. Over the past two decades, numerous successful demonstrations were reported on the design and fabrication of low-loss waveguides based on tellurite glasses [14], [15], [16], [17], [18].

$TeO_2$ glasses have a refractive index roughly around 2 @1550 nm [18], resulting in a relatively low index contrast when surrounded by silicon dioxide ($n \approx 1.45$ at 1550 nm). This index contrast imposes limitations on the compactness of photonic devices fabricated on this platform. For example, in silicon nitride ($n \approx 2$ at 1500 nm), bend radii of around 50 $\mu$m are typically required for 90° turns to minimize waveguide routing losses [19]. Inverse design has recently begun to transform the development of integrated photonic devices, enabling more compact and efficient components. Although most demonstrations of inverse design to date have focused on the SOI platform, recent work has extended its application to other materials, such as lithium niobate [20], silicon carbide [21], and silicon nitride [22], [23], [24], [25], demonstrating that inverse design is also effective for medium- to low-index contrast platforms.

In this work, we present two free-form devices designed for a 695 nm-thick tellurium dioxide glass platform (71% $TeO_2$ – 22.5% $WO_3$ – 5% $Na_2O$ – 1.5% $Nb_2O_5$): a TM-pass polarizer (TMPP) and a polarization beam splitter (PBS). Simulation results show an average transmission efficiency of −0.6 dB and an average polarization crosstalk of −24.3 dB for the TMPP across the C-band. For the PBS, the average efficiencies for the TE and TM modes are approximately −0.4 dB, with average

Received 27 September 2025; revised 13 November 2025; accepted 5 December 2025. Date of publication 15 December 2025; date of current version 23 December 2025. This work was supported in part by the Natural Sciences and Engineering Research Council of Canada (NSERC); in part by the Center for Optics, Photonics and Lasers (COPL); in part by the Regroupement Stratégique en Microsystémes du Québec (ReSMiQ); and in part by the Fundação de Amparo à Pesquisa do Estado de São Paulo (FAPESP). *(Corresponding author: Julian L. Pita.)*

Julian L. Pita and Michaël Ménard are with the Department of Electrical Engineering, École de Technologie Supérieure (ÉTS), Montreal, QC H3C 1K3, Canada (e-mail: julian-leonel.pita-ruiz@etsmtl.ca).

Jorge Diego Marconi is with CECS, Universidade Federal do ABC, Santo André, São Paulo 09210-580, Brazil.

Color versions of one or more figures in this letter are available at https://doi.org/10.1109/LPT.2025.3644331.

Digital Object Identifier 10.1109/LPT.2025.3644331

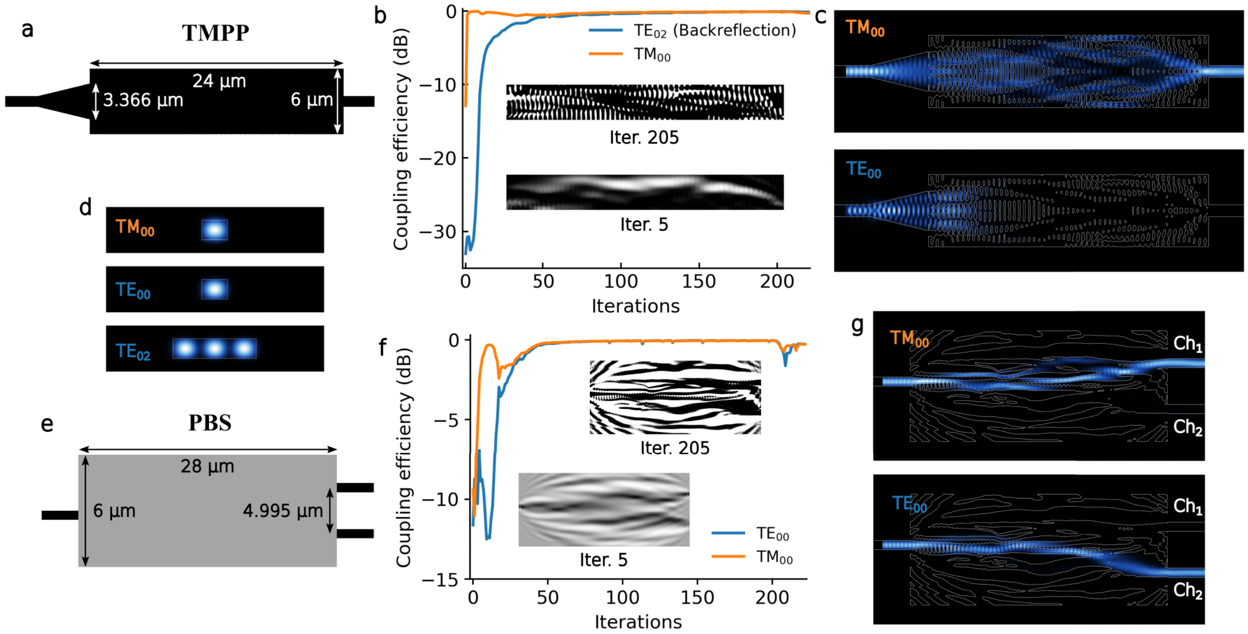

Fig. 1. Overview of the TMPP and PBS inverse design process. (a) and (e) Device schematics of the TMPP and PBS, showing the input and output waveguides and critical dimensions. Black regions represent tellurium dioxide ($TeO_2$), white regions represent silicon dioxide ($SiO_2$), and grey regions indicate an intermediate refractive indices corresponding to the average of these two materials. (b) and (f) Optimization trajectories for both devices, with insets showing intermediate geometries. (c) and (g) Simulated electromagnetic energy density at 1550 nm, overlaid with the final geometry for the TMPP and PBS, for the TE and TM modes in each device. (d) Electric field distributions of the modes used as input and output in the inverse design process.

crosstalk values of −19.4 dB and −31.2 dB across the entire C- and L-bands. Both devices play a crucial role in polarization control, as achieving pure TE or TM input/output modes is challenging on platforms with low refractive index contrast.

## II. DESIGN

During the design process, we employed the inverse design technique—specifically, a density-based topology optimization approach using the Python-based wrapper LumOpt. All devices feature a 695 nm-thick tellurium dioxide core, clad in silicon dioxide, with no intermediate etching steps, enabling a straightforward single-etch fabrication process. Thick waveguides are required for most tellurite-based nonlinear applications, as they are essential for accurately engineering dispersion and enhancing optical confinement. LumOpt leverages Ansys Lumerical 3D finite-difference time-domain (FDTD) to solve both the forward and adjoint problems for sensitivity analysis and employs gradient-based optimization algorithms from SciPy to drive the design evolution. The general inverse design problem, with the design variable $\rho$, is formulated as follows:

$$\underset{\boldsymbol{\rho}}{\text{minimize}} \quad f(\mathbf{E}(\boldsymbol{\rho})) \tag{1}$$

$$\text{subject to} \quad \nabla \times \left( \frac{1}{\mu_0 \mu_r} \nabla \times \mathbf{E} \right) - \omega_m^2 \epsilon_0 \epsilon_r(\boldsymbol{\rho}) \mathbf{E} = -i\omega_m \mathbf{J}, \tag{2}$$

$$0 \leq \boldsymbol{\rho} \leq 1 \tag{3}$$

$$g_k(\boldsymbol{\rho}) \leq 0, \quad k \in \{1, 2, \ldots, K\} \tag{4}$$

Eq. (1) defines $f$ as the objective function to be minimized. Eq. (2) governs the physics of the optimization, derived from Maxwell's equations. The material properties are determined by the density field $\boldsymbol{\rho}$—the design variable—bounded between 0 and 1 (Eq. (3)). Additionally, Eq. (4) introduces $g_k(\boldsymbol{\rho})$, representing fabrication-oriented inequality constraints on the material distribution. These constraints allow the definition of a minimum feature size, enabling the design of devices robust against fabrication variations. For complete mathematical details of the inverse design algorithms, including the topology optimization framework and sensitivity analysis methods, we refer readers to [26], [27], [28], and [29].

Fig. 1 presents the inverse design process of the TMPP and PBS. Figs. 1a and 1e show the main dimensions and initial conditions—the optimization region and refractive index distribution—of the inverse design process for both devices. Figs. 1b and 1f show the optimization trajectories, with two insets displaying intermediate geometries. Figs. 1c and 1g present the simulated energy density overlaid with the contour of the final geometry for both the TMPP and the PBS, whereas Fig. 1d displays the field distributions for the modes used in the design process. For both designs, we use the $TM_{00}$ and $TE_{00}$ modes of a 990 nm-wide input waveguide. In the case of the TMPP, the outputs are the transmitted $TM_{00}$ mode of a waveguide with the same width, and the reflected $TE_{02}$ mode in the 3.366 $\mu$m-wide output of a taper. For this device, in addition to reflecting the input TE mode, we convert it to a higher-order mode to minimize reflections into the input waveguide, and use the taper to further suppress the reflected TE mode. Optimization over the entire C-band was performed within a 24 $\mu$m × 6 $\mu$m design region, initialized with only $TeO_2$ material, as shown in Fig. 1a. The PBS was designed with the $TM_{00}$ and $TE_{00}$ input modes directed to separate 990 nm-wide output waveguides (channels 1 and 2, respectively). The spacing between the output waveguides

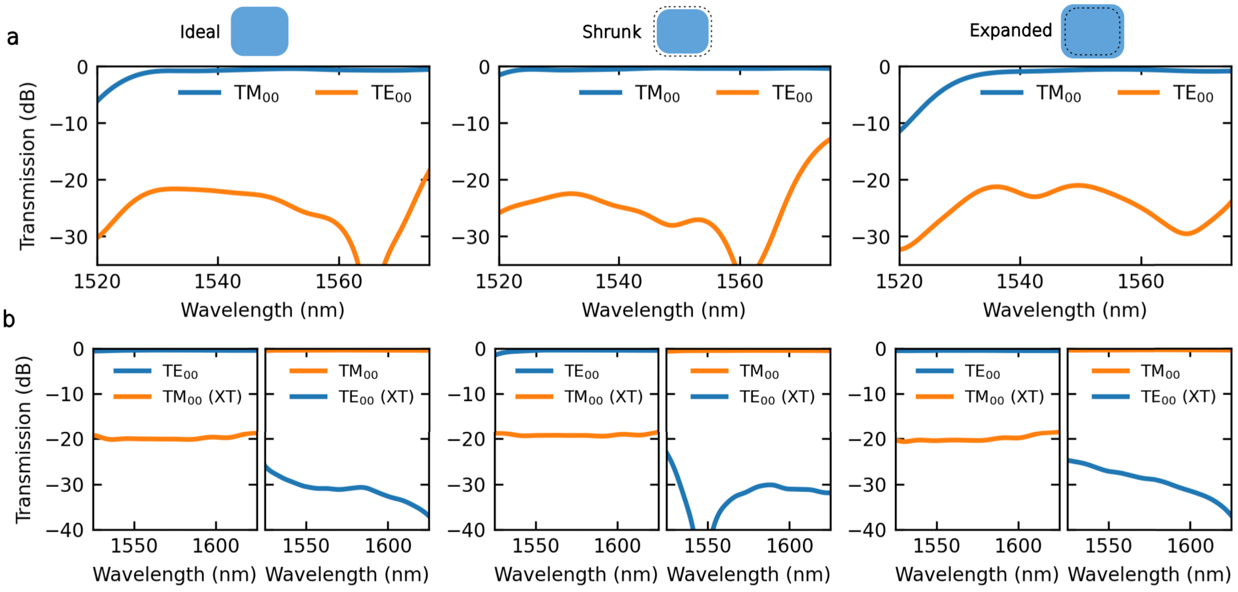

Fig. 2. Simulated transmission spectra of the devices with the ideal geometry and with fabrication variations of ±15 nm. (a) TM-pass polarizer and (b) polarization beam splitter. The right subfigure shows the transmission in Channel 1, while the left subfigure corresponds to Channel 2.

was set to 4.995 $\mu$m after running several optimizations with spacings ranging from 4.5 $\mu$m to 5.5 $\mu$m. The PBS inverse design was carried out in a 28 $\mu$m × 6 $\mu$m region (Fig. 1e), targeting broadband operation from 1520 nm to 1630 nm. A minimum feature size of 120 nm was enforced during both optimization processes.

The inverse design process consists of three stages. In the first stage, the refractive index is allowed to vary continuously between that of $TeO_2$ and $SiO_2$. In the second stage, the optimizer improves the figure of merit (FOM) while gradually driving the geometry toward a binarized refractive index distribution. In the third stage, design for the manufacturing (DFM) constraints are imposed to ensure compliance with fabrication limitations, enforcing a minimum feature size of 120 nm. Throughout all stages, a circular convolution filter with a radius of 120 nm and a projection function are applied to smooth the design region. For both the TMPP and the PBS, we used 30 iterations for the continuous stage. The binarization stage required 171 iterations for the TMPP and 166 iterations for the PBS, whereas the DFM stage took 19 and 26 iterations, respectively, as shown in Fig. 1b and 1f. The insets represent geometries from the first and third stages. It is worth noting that for the PBS, a slight drop in the optimization trajectory is observed in the third stage when the fabrication constraints are imposed. This could be because the stepwise increases of the binarization factor may not be sufficiently smooth. However, the FOM recovers to nearly its previous value by the end of the trajectory. Figures 1c and 1g show the simulated energy density distributions for both devices and both polarizations at 1550 nm. For the TMPP, the $TM_{00}$ mode passes through the device, while the $TE_{00}$ mode is converted to the $TE_{02}$ mode and reflected, then filtered out by the taper. In the case of the PBS, the polarization paths are clearly separated and directed to their corresponding output channels.

## III. RESULTS

In this section, we present the simulation results for each ultra-compact freeform device, along with an analysis of their robustness to fabrication variations. Specifically, we examine two cases: lateral over-etching (shrinking) and lateral under-etching (expansion). The freeform TMPP and PBS devices function as subwavelength optical systems that precisely engineer light–matter interactions. Their non-intuitive geometries enable spatial control of the effective refractive index distribution, creating tailored patterns of constructive and destructive interference. These patterns are optimized for specific wavelengths, modes, and polarization states, demonstrating the power of inverse design in nanophotonics—particularly for platforms with moderate to low refractive-index contrast.

Fig. 2a shows the performance of the TMPP across the C-band, whereas Fig. 2b presents the performance of the PBS across both C- and L-bands. For the TMPP with the ideal design, the simulated average transmission efficiency over the C-band is approximately −0.6 dB for the $TM_{00}$ mode and −24.9 dB for the $TE_{00}$ mode. Notably, below 1530 nm, the $TM_{00}$ transmission drops to around −6.1 dB, while the $TE_{00}$ transmission decreases to approximately −29.9 dB, maintaining a polarization crosstalk below −23.8 dB. For the PBS, Channel 2 shows an average $TE_{00}$ transmission efficiency of −0.4 dB with undesired $TM_{00}$ transmission of approximately −19.8 dB across the entire spectral range for the ideal design. Channel 1 exhibits an average $TM_{00}$ efficiency of −0.4 dB with undesired $TE_{00}$ transmission of approximately −31.6 dB. While the undesired transmission in Channel 2 remains relatively constant over the full simulated band, in Channel 1 it decreases with increasing wavelength.

We further investigated the robustness of both devices to fabrication variations, considering lateral over-etching and under-etching of approximately 15 nm. For the TMPP, the modeled over-etching shifts the $TM_{00}$ transmission spectrum toward shorter wavelengths, improving the average $TM_{00}$ transmission to −0.4 dB and eliminating the efficiency drop below 1530 nm observed in the ideal case. The polarization crosstalk remains below −21.8 dB across the entire C-band. Since the design outcome is nearly, but not perfectly, binary, the over-etched device exhibits slightly improved performance in the C-band, as the geometry can be fine-tuned to enhance robustness against fabrication variations, with only a marginal trade-off in nominal performance. In contrast, under-etching shifts the $TM_{00}$ spectrum toward longer wavelengths, reducing the $TM_{00}$ transmission to approximately −11.3 dB at shorter wavelengths, while the $TE_{00}$ transmission decreases to about −32.2 dB. The average TMPP efficiency drops to −0.9 dB, while maintaining crosstalk below −20.2 dB. For the PBS, over-etching keeps the average $TE_{00}$ transmission in Channel 2 nearly unchanged, while decreasing the $TM_{00}$ transmission in Channel 1 to −0.5 dB, with crosstalk remaining below −17.9 dB and −26.9 dB for Channels 2 and 1, respectively, in the C-band. Under-etching improves the average $TM_{00}$ transmission in Channel 1 to −0.3 dB, while other performance metrics remain similar to those of the ideal geometry. Overall, the devices demonstrate superior robustness to over-etching compared to under-etching scenarios, confirming the structural resilience of the designs against fabrication tolerances up to 15 nm. Moreover, when compared to their silicon nitride counterparts [24], the presented devices exhibit improved polarization crosstalk, achieving values even below −30 dB.

## IV. CONCLUSION

In summary, we demonstrated, through numerical simulations, two ultra-compact freeform devices—a TMPP and a PBS—in tellurium oxide using inverse design methods. These optimized structures achieve record performance metrics in $TeO_2$ platforms across the C- and L-bands while maintaining insertion losses below 1 dB. Tolerance analysis confirms strong robustness to fabrication variations, preserving target performance across ±15 nm lateral etching deviations. This work paves the way for high-density integration in photonic circuits and establishes tellurite glass as a versatile platform for passive devices beyond conventional active components.

## REFERENCES

[1] W. Blanc et al., “The past, present and future of photonic glasses: A review in homage to the united nations international year of glass 2022,” *Prog. Mater. Sci.*, vol. 134, Apr. 2023, Art. no. 101084.

[2] L. Verger et al., “Preparation and characterizations of glasses in the $TeO_2$-$Ga_2O_3$–$M_2O$ (M = Li, Na, K) systems,” *Int. J. Appl. Glass Sci.*, vol. 15, no. 3, pp. 203–211, 2024.

[3] A. Shearer, B. Hauke, M. Montazerian, and J. C. Mauro, “A critical review of infrared transparent oxide glasses,” *Opt. Mater., X*, vol. 20, Dec. 2023, Art. no. 100258.

[4] S. J. Madden and K. T. Vu, “High-performance integrated optics with tellurite glasses: Status and prospects,” *Int. J. Appl. Glass Sci.*, vol. 3, no. 4, pp. 289–298, Dec. 2012.

[5] H. Mbonde et al., “Demonstration of passive, nonlinear and active devices on a hybrid photonic platform,” *Opt. Exp.*, vol. 33, no. 1, pp. 1836–1847, Dec. 2025.

[6] A. Boussetta et al., “Investigation of thermal and spectroscopic properties of tellurite-based glasses doped with rare-Earth oxides for infrared solid-state lasers,” *Materials*, vol. 17, no. 15, p. 3717, Jul. 2024.

[7] M. P. Belançon, J. D. Marconi, M. F. Ando, and L. C. Barbosa, “Near-IR emission in $Pr^{3+}$ single doped and tunable near-IR emission in $Pr^{3+}/Yb^{3+}$ codoped tellurite tungstate glasses for broadband optical amplifiers,” *Opt. Mater.*, vol. 36, no. 6, pp. 1020–1026, Apr. 2014.

[8] D. Vinay et al., “Silver oxide embedded alkali zinc boro tellurite glasses: Physical, structural and optical properties for possible optical switching applications,” *J. Mol. Struct.*, vol. 1339, Sep. 2025, Art. no. 142388.

[9] R. Deb and P. S. Maji, “Investigation of parametric gain and bandwidth of tellurite hybrid micro-structured fiber with four ZDWs,” *Opt. Quantum Electron.*, vol. 53, no. 12, p. 717, Dec. 2021.

[10] M. Evrard et al., “Dispersion-shifted tellurite fibers for nonlinear frequency conversion,” *Opt. Mater., X*, vol. 15, Aug. 2022, Art. no. 100183.

[11] E. Krutova et al., “Supercontinuum generation in a graded-index multimode tellurite fiber,” *Opt. Lett.*, vol. 49, no. 11, pp. 2865–2868, 2024.

[12] F. Désévédavy et al., “Review of tellurite glasses purification issues for mid-IR optical fiber applications,” *J. Amer. Ceram. Soc.*, vol. 103, no. 8, pp. 4017–4034, Aug. 2020.

[13] D. Munoz-Martin et al., “Structural and optical properties of tellurite thin film glasses deposited by pulsed laser deposition,” *Thin Solid Films*, vol. 520, no. 1, pp. 131–137, Oct. 2011.

[14] N. Wei, X. Li, J. He, Y. Fan, Y. Dan, and J. Wang, “Design of an optical slot waveguide amplifier based on $Er^{3+}$-doped tellurite glass,” *Chin. Opt. Lett.*, vol. 21, no. 1, 2023, Art. no. 011404.

[15] J. L. Clabel Huamán, K. T. de Paula, F. A. Couto, G. Lozano Calderón, J. D. Vollet-Filho, and C. R. Mendonça, “Enhancing waveguide performance in $La^{3+}$-Doped tellurite glasses: Energy-induced structural tuning for reduced propagation loss,” *ACS Omega*, vol. 10, no. 22, pp. 23696–23708, Jun. 2025.

[16] E. A. M. Fagotto et al., “Impact of wideband wavelength conversion on the performance of optical networks,” *Opt. Laser Technol.*, vol. 169, Feb. 2024, Art. no. 109948.

[17] I. Bányász et al., “Characterisation of channel waveguides fabricated in an $Er^{3+}$-doped tellurite glass using two ion beam techniques,” *Chemosensors*, vol. 10, no. 8, p. 337, Aug. 2022.

[18] J. D. Marconi, M. L. F. Abbade, C. M. Serpa-Imbett, and E. A. M. Fagotto, “Ultra-broadband two-pump optical parametric amplifier in tellurite waveguides with engineered dispersion,” *Opt. Exp.*, vol. 25, no. 4, pp. 4268–4283, 2017.

[19] J. L. P. Ruiz, N. Dalvand, and M. Ménard, “Inverse-designed 90-degree silicon nitride bends for the C band,” *J. Lightw. Technol.*, vol. 43, no. 12, pp. 5804–5810, Jun. 15, 2025.

[20] C. Shang et al., “Inverse-designed lithium niobate nanophotonics,” *ACS Photon.*, vol. 10, no. 4, pp. 1019–1026, Apr. 2023.

[21] J. Yang, M. A. Guidry, D. M. Lukin, K. Yang, and J. Vučković, “Inverse-designed silicon carbide quantum and nonlinear photonics,” *Light, Sci. Appl.*, vol. 12, no. 1, p. 201, Aug. 2023.

[22] J. L. Pita Ruiz, F. Nabki, and M. Ménard, “Silicon nitride TM-pass polarizer using inverse design,” *Opt. Exp.*, vol. 31, no. 23, pp. 37892–37899, 2023.

[23] J. Pita, F. Nabki, and M. Ménard, “Inverse-designed silicon nitride reflectors,” *Opt. Lett.*, vol. 49, no. 4, pp. 786–789, 2024.

[24] J. L. Pita Ruiz, N. Dalvand, and M. Ménard, “Integrated silicon nitride devices via inverse design,” *Nature Commun.*, vol. 16, no. 1, p. 9307, Oct. 2025.

[25] T. Fu, Z. Ma, X. Yan, X. Zhang, and X. Ren, “Inverse-designed non-uniform silicon nitride gratings with high beam steering performance,” *IEEE Photon. J.*, vol. 15, no. 2, pp. 1–8, Apr. 2023.

[26] J. S. Jensen and O. Sigmund, “Topology optimization for nano-photonics,” *Lase Photon. Rev.*, vol. 5, no. 2, pp. 308–321, 2010.

[27] O. Sigmund and K. Maute, “Topology optimization approaches: A comparative review,” *Structural Multidisciplinary Optim.*, vol. 48, no. 6, pp. 1031–1055, Dec. 2013.

[28] F. Wang, B. S. Lazarov, and O. Sigmund, “On projection methods, convergence and robust formulations in topology optimization,” *Structural Multidisciplinary Optim.*, vol. 43, no. 6, pp. 767–784, Jun. 2011.

[29] R. E. Christiansen and O. Sigmund, “Inverse design in photonics by topology optimization: Tutorial,” *J. Opt. Soc. Amer. B, Opt. Phys.*, vol. 38, no. 2, pp. 496–509, 2021.